Aeroacoustic simulations of two co-rotating propellers at low Reynolds number with installation effects

S. Le Bras, K. Kucukcoskun, D. Acevedo-Giraldo, M. Roger

Accepted version for publication in Journal of Sound and Vibration

Link to published version: https://doi.org/10.1016/j.jsv.2025.119248

Aeroacoustic simulations of two co-rotating propellers at low Reynolds number with installation effects

S. Le Bras[a,*,1], K. Kucukcoskun[b], D. Acevedo-Giraldo[c] and M. Roger[c]

[a] *Siemens Digital Industries Software, 107 Avenue de la République, 92320 Châtillon, France*

[b] *Siemens Digital Industries Software, Interleuvenlaan 68, 3001 Leuven, Belgium*

[c] *Univ Lyon, École Centrale de Lyon, CNRS, Univ Claude Bernard Lyon 1, INSA Lyon, LMFA, UMR 5509, 36 Avenue Guy de Collongue, 69130 Écully, France*

ARTICLE INFO

Keywords:
aeroacoustics
propeller noise
distributed electric propulsion
installation effects
incompressible simulations
large-eddy simulation
high-order finite element method

ABSTRACT

In this study, the sound radiated by two co-rotating propellers mounted side-by-side in close proximity is investigated numerically under low Reynolds number conditions. The pylon-mounted propellers, previously studied experimentally in the literature, are representative of the propellers equipping distributed electric propulsion architectures for aircraft. They consist of six-blade XPROP-S propellers operating at a rotational speed of 7000 rpm with constant pitch angle. Operating conditions at zero advance ratio are considered. The numerical simulations are carried out using a two-step hybrid approach. In the first step, an incompressible large-eddy simulation is performed to compute the flow field. In the second step, tonal and broadband noise predictions with installation effects are obtained using a high-order finite-element approach. The performance of the numerical approach is first verified for a single pylon-mounted propeller. The numerical methodology is then applied to the two-propeller configuration. Acoustic results are successfully compared to experimental data from the literature and further insights into the sound generation mechanisms are provided. In particular, for this zero-advance-ratio propeller configuration, the importance of accounting for propeller-propeller aerodynamic interactions to obtain accurate noise predictions is highlighted. Including installation effects in the acoustic simulations is also found to improve the predictions in the low frequency range.

1. Introduction

With the constant growth of civil air transportation and the need to reduce carbon emissions, particular attention has been given to disruptive electric propulsion technologies for aircraft during the past few years. Amongst the new foreseen propulsion systems, Distributed Electric Propulsion (DEP), consisting of multiple propellers installed throughout the aircraft, raises particular interest [1]. One of the main challenges of DEP is the design of quieter systems, especially as they involve complex and not always well-understood aerodynamic and aeroacoustic installation effects. In this context, the noise footprint of the propulsion system can therefore no longer be studied and optimized separately from its installation. In particular, a good knowledge of the flow features introduced by the aerodynamic and acoustic interactions is needed at the very early design stages.

The effect of propeller-propeller interactions on the aerodynamic performance and on the noise footprint of the DEP configurations have been the subject of several experimental and numerical recent studies [2, 3]. In particular, in the literature, it is reported that when propellers are in close proximity, typically with separation distances below 0.4 propeller diameter, the unsteady loading induced by rotor interactions can lead to a significant increase in the

*Corresponding author
sophie.le_bras@siemens.com (S. Le Bras)
ORCID(s): 0000-0001-7859-2569 (S. Le Bras)

sound levels, especially in the normal direction of the rotor plane [3]. In this study, the influence of propeller-propeller interactions on noise is studied numerically for a two XPROP-S propeller arrangement [4], previously studied experimentally at École Centrale de Lyon (ECL) [5, 6] in the context of ENODISE European project [7]. Such configuration is representative of propellers in DEP aircraft architectures. It includes two co-rotating propeller units, synchronized and mounted side-by-side on their frame, as illustrated in Fig. 1. Here the frame refers to the pylon-and-hub assembly. The separation distance between the adjacent propeller tips is of 6.8 mm, corresponding to $0.033\boldsymbol{D}$, with $\boldsymbol{D}$ the propeller diameter.

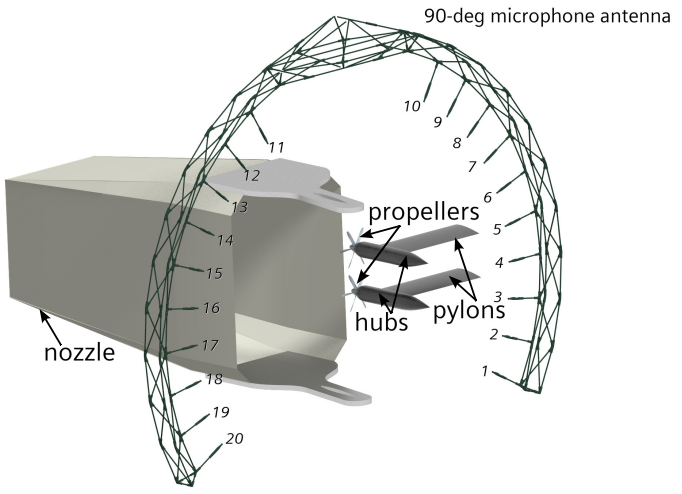

Figure 1: Distributed XPROP-S propeller configuration of the ECL test campaign, with microphones indexed from 1 to 20 [5, 6].

Aeroacoustic simulations of distributed XPROP-S propellers have already been reported in the literature, but mainly in forward-flight conditions [8, 9, 10] with a free-stream velocity of 30 m/s and a tip-to-tip separation distance of 0.02 $\boldsymbol{D}$, according to the authors' knowledge. In this work, zero-advance ratio conditions, representative of static operation before take-off, are considered instead. Such conditions are particularly interesting for this DEP configuration as they have been found to be substantially louder than in-flight conditions in the ECL experiment [5].

In order to perform accurate aeroacoustic simulations of propellers at low-Mach number flows at a reasonable computational cost, it is common to use hybrid methods and to decompose the overall aeroacoustic problem into sub-problems solved with different methods [11]. Assuming a one-way fluid-to-acoustic coupling, the flow field can be computed separately from the acoustic field using an incompressible CFD simulation which is less computationally intensive than a compressible one. The flow data can then be used to define sound sources for the acoustic simulation [12]. Depending on the application of interest, such acoustic propagation simulation can be performed in the time domain or in the frequency domain, with analytical acoustic analogies or numerical discretization of the propagation equations. When the far-field scattering from arbitrary neighboring surfaces is also a concern, numerical propagation models, like frequency-domain finite-element approaches, are often preferred. Such a strategy is applied in the present study.

From a CFD simulation perspective, the prediction of the aerodynamic noise from small propellers operating at low Reynolds numbers below 5×10^5 is challenging, due to complex boundary-layer phenomena like transition or laminar separation [13, 14]. In this work, as an attempt to accurately capture the propeller aerodynamics, the flow field is computed using an incompressible Large-Eddy Simulation (LES). The flow simulation is carried out with the finite-volume CFD software Simcenter STAR-CCM+ [15], widely used during the past years for hybrid methods based on incompressible flows to simulate a variety of applications like HVAC noise [16], fan noise [17], side mirror noise [18] or academic test cases [19]. The acoustic simulation, accounting for installation effect, is then carried out using a frequency-domain high-order Finite-Element (FE) method [20] available in Simcenter 3D Acoustics [21]. The focus is put on propeller loading noise, the sources of which are equivalent dipoles, according to Ffowcs Williams & Hawkings' formulation of the acoustic analogy. Indeed, at the considered subsonic Mach numbers, quadrupole noise is

considered as negligible. Furthermore, thickness noise plays a minor role for thin blades. The FE simulation is achieved by decomposing the propeller blades into compact segments assimilated to rotating dipoles.

This LES-FE approach is first applied to a single propeller mounted on its frame. The system is considered at zero advance ratio to demonstrate feasibility in a relatively simple case, which already includes a minimum installation effect caused by the frame. The purpose of the single-propeller study is twofold: assessing the accuracy of the numerical approach by means of comparisons against the measurements of the ECL test campaign [5, 6], and studying the relative noise contributions of the propeller and its frame in this simple case.

The applicability of the present numerical approach to the two-propeller DEP configuration is then investigated. The focus is put on the additional noise contributions associated with propeller-propeller interactions. To highlight the importance of propeller-propeller aerodynamic interactions, acoustic simulations are carried out with and without accounting for these interactions. In practice, in order to discard these interactions, aerodynamic noise sources from a single-propeller flow simulation are duplicated to mimic the presence of the second propeller.

The paper is organized as follows. The computational strategy used to predict propeller noise with installation effects is first described in Sec. 2. Its application to a single pylon-mounted XPROP-S propeller is presented in Sec. 3. Finally, the applicability of the methodology to a distributed propeller configuration is demonstrated in Sec. 4.

2. Numerical approach

The numerical strategy adopted here consists of a two-step hybrid approach. In a first step, a three-dimensional incompressible LES simulation of the propellers installed on their frames is carried out in order to compute the propeller aerodynamic noise sources. In a second step, a FE acoustic simulation is performed in order to predict the radiated noise.

2.1. Incompressible LES simulations

The incompressible LES simulation is performed using the unsteady segregated flow solver available in CFD software Simcenter STAR-CCM+ [15], with the constant density equation of state. It is carried out using the Wall Adaptive Local Eddy-viscosity (WALE) subgrid scale model [22]. The flow is solved based on the SIMPLEC algorithm and an implicit second order backward differencing scheme in time. For the discretisation of the convective fluxes, a hybrid MUSCL third-order/central-differencing discretization scheme is used. The numerical dissipation of the scheme is adjusted by an upwind blending factor varying between 0 and 1. This factor is set to 0.1 in order to maximize accuracy. The least-square gradient reconstruction approach is used with the Venkatakrishnan limiter method. The rotation of the propeller is modelled using a moving-mesh approach relying on the rigid body motion model available in Simcenter STAR-CCM+.

2.2. Acoustic simulations

2.2.1. Acoustic predictions with installation effect

The propeller loading noise approach [23] used in this work is based on sound sources modelled as discrete dipoles. The rotor blades are first decomposed into compact segments. The segment length, denoted L_s, is defined as a function of the speed of sound c_0 and the maximum frequency of interest $f_{\max}$ for the noise predictions:

$$L_s = \frac{c_0}{N_s f_{\max}} \tag{1}$$

where N_s is the number of segments per acoustic wavelength. Setting $N_s = 4$ led to accurate results for various types of rotors [23, 24] and is also used here. Each segment is modelled as a rotating dipole located at the center of gravity of the segment. The dipole strengths are then obtained by integration of the CFD unsteady incompressible pressure over the surface of the segments.

Tonal and broadband noise predictions including installation effect are computed by solving a Helmholtz problem. Mean flow convection and refraction effects on the sound propagation are neglected. This is justified in the present case, because zero advance-ratio is considered, on the one hand, and because the local refraction effects in the very vicinity of the blades are negligible at the low reached blade-tip Mach number of about 0.2, on the other hand. The Helmholtz equation is discretized using the high-order frequency-domain Finite Element Method Adaptive Order (FEMAO) approach [20] available in Simcenter 3D Acoustics [21]. FEMAO is based on a high-order continuous Galerkin finite element method equipped with a basis of integrated Legendre polynomials. Such an approach provides substantial

reductions in memory and CPU time compared to conventional finite elements for acoustic applications [20]. To account for installation effects, the FE simulations can include scattering by rigid or lined surfaces of arbitrary geometries.

In order to mimic the propeller rotation, the dipoles rotate according to the time discretization used in the CFD simulation. In practice, at a given time step, the dipole strength is mapped onto the local Degrees of Freedom (DoFs) of the high order element met on the dipole's trajectory. The time signal thus obtained for each high-order DoF is Fourier-transformed and then used as a source term in the FE problem.

The FE simulation can also account for the flow-generated sound sources at the scattering surfaces using a Curle's acoustic analogy [12], adapted to be used with the unsteady incompressible aerodynamic pressure obtained from the CFD simulation.

2.2.2. Acoustic predictions in free field

When the acoustic installation effect can be neglected, the tonal and broadband loading noise emitted by a propeller radiating in free-field can be accurately computed using a fast-turn around analytical approach informed by CFD. The sound field is then assimilated to the noise of dipoles radiating in free field. The analytical model is briefly recalled below.

An expression for the acoustic pressure of a dipole in arbitrary subsonic motion at an observer position $\mathbf{x}$ can be derived from the loading-noise term in the Ffowcs Williams and Hawkings [25] equation:

$$p(\mathbf{x},t) = \frac{1}{4\pi}\frac{\partial}{\partial x_i}\left[\frac{F_i}{RD_f}\right] \tag{2}$$

where R is the distance between the dipole and the observer, $D_f = 1-(\mathbf{M}\cdot\mathbf{R}/R)$ is the Doppler factor, $\mathbf{M}$ is the Mach number vector, $\mathbf{R}$ is the dipole-observer distance vector and F_i are the dipole force components. The squared brackets in Eq. (2) stand for a retarded-time evaluation. We further assume that the dipole follows a circular path and adopt the convention of notation $\mathrm{e}^{+\mathrm{i}\omega t}$ for monochromatic waves, so that the time Fourier transform of the acoustic pressure reads

$$\hat{p}(\mathbf{x},\omega) = \frac{1}{T}\int_0^T p(\mathbf{x},t)\mathrm{e}^{-\mathrm{i}\omega t}\mathrm{d}t \tag{3}$$

where ω is the angular frequency at which the acoustic field is computed, T is the duration of the time signal p which usually corresponds to a few rotations. This yields the expression:

$$\hat{p}_{\text{analytical}}(\mathbf{x},\omega) = \frac{\mathrm{i}k}{4\pi T}\int_0^T \frac{\mathbf{F}\cdot\mathbf{R}}{R^2}\left(1+\frac{1}{\mathrm{i}kR}\right)\mathrm{e}^{-\mathrm{i}\omega(\tau+R/c_0)}\mathrm{d}\tau \tag{4}$$

where $\mathbf{F}$ is the dipole strength computed from CFD data for each compact blade segment, $k=\omega/c_0$ and c_0 is the speed of sound. Equation (4) corresponds to the expression derived by Roger [26], up to differences related to a different convention for the time Fourier transform.

3. Application to a XPROP-S propeller

3.1. Description of the isolated propeller configuration

The configuration studied in this work reproduces the conditions of the ECL experimental campaign [5]. It consists of a pylon-mounted six-blade XPROP-S propeller of 0.2032 m diameter operating at a rotational speed of 7000 rpm with constant pitch angle. Views of the XPROP-S propeller and the experimental setup are provided in Fig. 2. Details about the geometry of the propeller can be found in reference [4]. The operating condition at zero advance ratio ($J=0$) is considered. It corresponds to the operating point 66 in the ECL experimental database published in Zenodo [6]. The propeller rotates clockwise as viewed from the front. The main test conditions of this propeller configuration are reported in Tab. 1. The chord-based Reynolds number at blade tip is of about 3.2×10^4, in the transitional range. In the ECL experiment [5], the microphone antenna shown in Figs. 2(b) and 2(c) rotates around the vertical axis to cover a portion of a sphere around the propeller. In this work, for the sake of brevity, comparisons between simulation and test results for the single-propeller case are mainly presented when the antenna is in the plane normal to the propeller axis, at 0.1 m downstream of the rotor plane for the single propeller. This corresponds to the 90° antenna position in

Fig. 2(c). The distance between the center of the microphone arc and the center of the rotor in the radial direction is of about 0.015 m. This offset is due to the fact that the vertical antenna axis in Fig. 2(b) coincides with the trailing edge of a wing mounted in other setup configurations, not addressed in the present work.

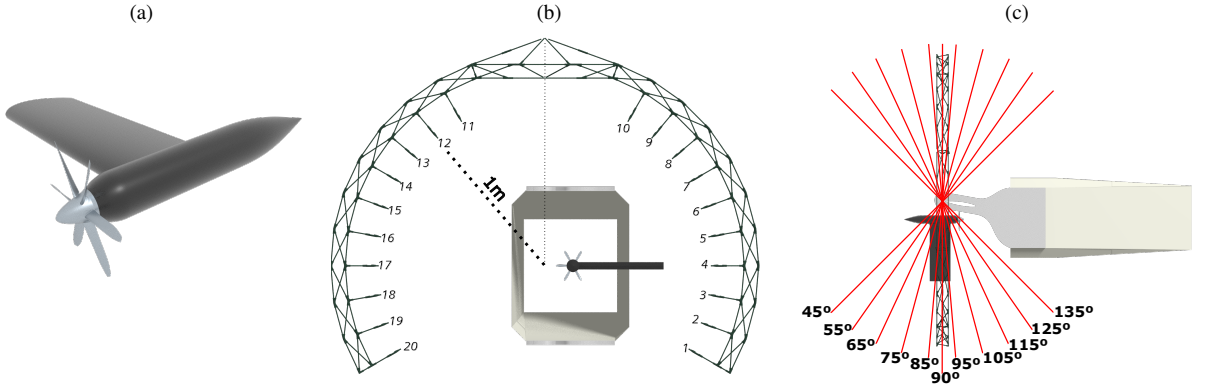

Figure 2: Representation of (a) the XPROP-S propeller installed on its frame composed of a hub and pylon, (b) back view and (c) top view of the ECL experimental setup for single propeller. 90° antenna position located at 0.1 m downstream of the rotor plane for single propeller. Angular distance between microphones of 10°, with microphones 4 and 17 at 0° and 180° respectively in the plane of the pylon.

Table 1
Main operating conditions of the XPROP-S propeller configuration.

Experimental operating point [6]	n°66
Propeller model	XPROP-S [4]
Rotor diameter [m]	0.2032
Blade chord at the tip [m]	6.9×10^{-3}
Blade chord at the root [m]	1.6×10^{-2}
Number of blades	6
Advance ratio J	0
Flight stream velocity U_∞ [m/s]	0
Rotational speed [rpm]	7000

3.2. Numerical setup

3.2.1. LES setup

The CFD domain used for the LES simulation is presented in Fig. 3(a). It is made of a cylindrical rotating region surrounding the propeller and of a stationary region in the rest of the domain. A polyhedral mesh of about 28 M cells is designed for the LES simulation. The mesh is refined in the rotating area in order to capture the sound sources in the vicinity of the propeller blades. In particular, the mesh verifies $y^+ < 5$ at the blades walls, with 15 prism layers and a cell size of 10^{-5} m in the wall-normal direction. A view of the LES polyhedral mesh and the wall y^+ values on a blade is given in Fig. 3(b).

In order to overcome the fine mesh requirements of wall-resolved LES at the surface of the propeller frame, wall modelling based on Reichardt's law [27, 17] is applied, which enables us to use a coarser mesh in this region, with $y^+ < 50$ at the pylon, and $y^+ < 80$ at the hub. The simulation is performed with 4320 time steps per propeller revolution in order to ensure low CFL values at the blade tips. The simulation is first initialized for eight propeller revolutions. The unsteady incompressible pressure data are then recorded for a duration of 16 revolutions at a sampling frequency of 84 kHz. The LES simulation has been performed on AMD EPYC 7532 ROME CPU processors, using a total of 768 compute cores. About 220 000 CPU hours have been used for the simulation. It is important to mention that this simulation has not been optimized for optimal run time (mesh and timestep-wise).

Flow simulations have also been performed with coarser and finer grids to verify that the acoustic results are independent of the mesh resolution, as reported in Appendix A.

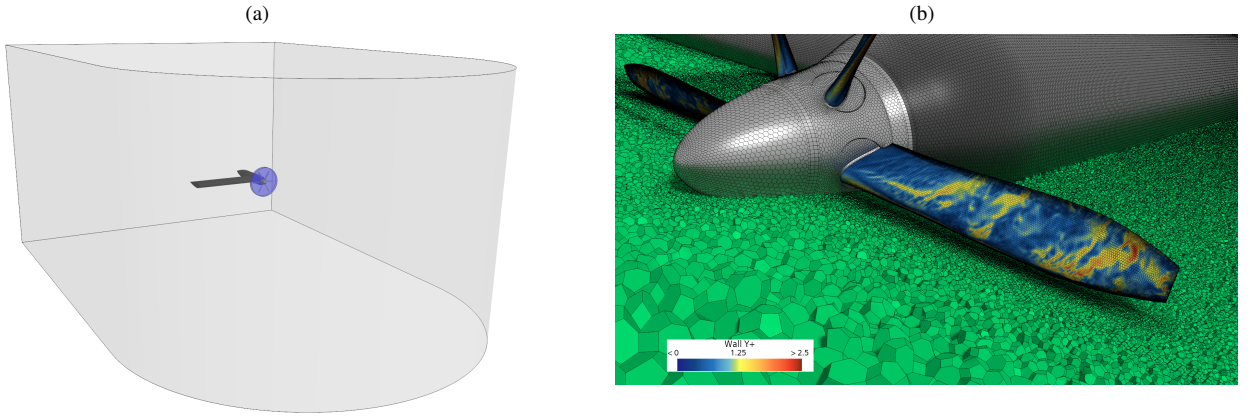

Figure 3: Views of (a) the CFD domain considered for the LES simulation of the isolated XPROP-S propeller and (b) the LES polyhedral mesh and wall y^+ values on a blade.

3.2.2. Finite element simulation setup

Acoustic predictions have been been computed for four configurations illustrated in Fig. 4: (a) propeller radiating in free-field with no contribution from the scattering surface, (b) propeller radiating in the presence of the frame considered only as a scattering surface, (c) propeller radiating in the presence of the frame considered as a scattering surface and a source, and (d) frame radiating with no account for the propeller.

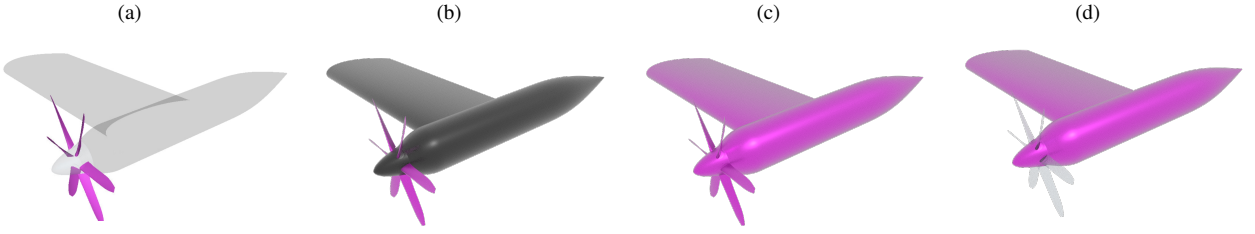

Figure 4: View of the four single-propeller configurations considered in acoustic simulations, with aerodynamic source components indicated in purple and scattering surfaces indicated in black: (a) propeller noise in free-field, (b) propeller noise and frame as a scattering surface, (c) propeller noise and frame as noise source and scattering surface and (d) frame as noise source and scattering surface.

Noise predictions with installation effects have been computed with FEMAO [20] over the frequency range 100 Hz $\leq f \leq$ 6 kHz, whereas free-field predictions have been calculated analytically from Eq. (4) up to 12 kHz. As described previously in Sec. 2.2, the propeller blades are decomposed into compact segments which are modelled as rotating dipoles. The blade segment length L_s is defined from Eq. (1). For a maximum frequency of interest of 12 kHz, this yields $L_s \simeq 7$ mm, which corresponds to about 24 dipoles per blade, as illustrated in Fig. 5. A view of the FE domain and surface mesh with frame is presented in Fig. 6(a), together with the microphone arc where acoustic results are computed. For computational efficiency, the FE domain is restricted to a small region which surrounds the frame-mounted propeller but does not include the microphone arc. At the external boundary of the domain, an Automatically Matched Layer (AML) [28] made of seven layers is used to absorb outgoing waves (not shown in Fig. 6(a)). Acoustic results at the microphone arc are obtained using a Kirchhoff extrapolation fed with the acoustic data at the AML.

The FE mesh is made of tetra10 quadratic elements in order to accurately represent the geometry of the propeller frame (hub and pylon). Element sizes are of 0.006 m near the propeller and at the frame surface, and of 0.04 m at the

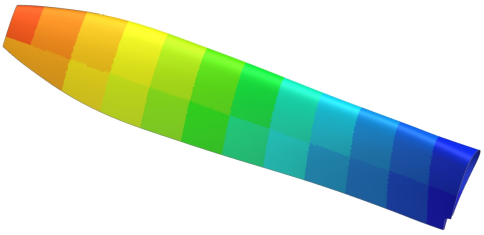

Figure 5: Propeller blade segmentation used to compute the aerodynamic loads for the acoustic simulations. Each compact segment is then modelled as a rotating dipole.

external boundaries of the domain. A cylindrical area is created around the propeller in order to better control the mesh resolution in this sound-source region. This precaution, not fundamentally needed in practice, is adopted here in order to ensure that the spatial resolution of the propeller sound sources is the same for the different installed configurations of Fig. 4.

From a practical point of view, only one mesh per propeller configuration has to be generated, for the complete range of frequencies. Indeed, FEMAO is taking care of automatically adjusting the polynomial order p_{FEM}, based on the frequency, the local grid size and the local medium properties, so as to achieve a user-defined accuracy [20]. This is illustrated in Figs. 6(b) and 6(c) where the FE order distributions in the horizontal propeller meridian plane are shown at the Blade Passing Frequency (BPF) and at $f = 5\mathrm{BPF}$, respectively. At these frequencies, the order p_{FEM} varies between 2 and 8.

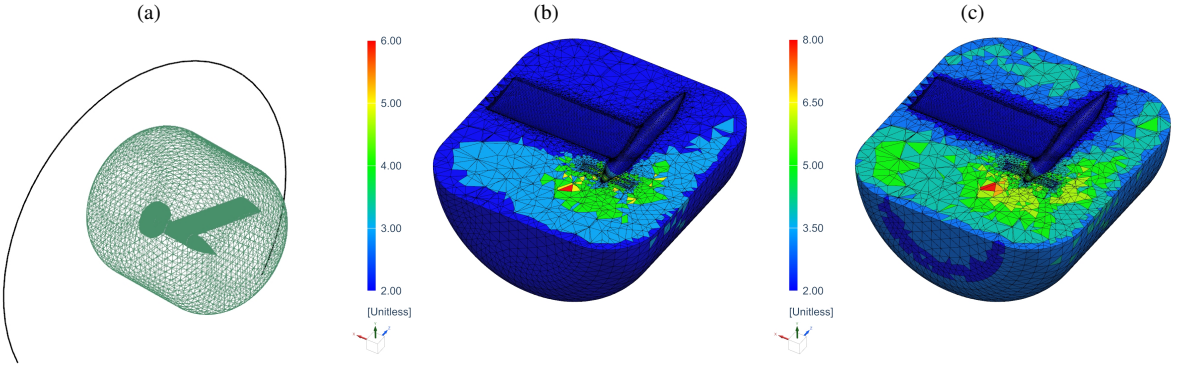

Figure 6: Views of (a) the FE domain and 90° microphone arc in the study of the pylon-mounted propeller, and distribution of FEMAO orders p_{FEM} in propeller axis plane at (b) $f = \mathrm{BPF}$ and at (c) $f = 5\mathrm{BPF}$.

The acoustic simulations have been carried out using a PowerEdge R640 compute node with 2 Intel Xeon Gold 6246R 3.4G 16-core processors with 1.5 Tb memory available. Information about memory requirements and FE orders for the acoustic simulations at $f = 5950$ Hz are provided in Tab. 2. At this frequency, about 70 Gb of RAM are required to solve the FE problem with propeller noise sources. The FEM polynomial order reaches a maximum value of 10 in the free-field configuration, where the mesh includes larger elements in the absence of frame.

In order to improve the statistical convergence of the acoustic results, the acoustic spectra are computed following a Welch's method. The transient source signals are split into blocks of two propeller revolutions which overlap by 50 %. This results into a frequency resolution of 58.3 Hz for the acoustic spectra. For reliable test/simulation comparisons, the experimental spectra have been calculated with the same frequency resolution as for the numerical spectra.

The accuracy of the FEMAO formulation has been verified for the free-field propeller configuration by comparing the numerical results with the analytical solution in Appendix B. An excellent match is obtained between the FE and the analytical results.

Table 2
Information about in-core solver memory requirements and maximum FEMAO order to solve the FE problems at $f = 5950$ Hz for single-propeller configurations.

Configuration	Required memory (RAM)	Maximum p_{FEM} order
Propeller noise in free field	69.7 Gb	10
Propeller noise and frame as a scattering surface	77.2 Gb	9
Propeller noise and frame as noise source and scattering surface	77.2 Gb	9
frame-only as noise source and scattering surface	37.5 Gb	8

3.3. Aerodynamic results

3.3.1. Flow instantaneous views

Instantaneous views of vorticity isocontours colored by the velocity magnitude are presented in Fig. 7. In the absence of flight stream, tip-vortices cannot be strongly convected downstream of the propeller. They stay in the propeller plane, slightly drifting at much lower speed than the blade-tip motion. This leads to a strong interaction of the blades with their wakes and tip-vortices, in addition to the interaction with the frame further downstream.

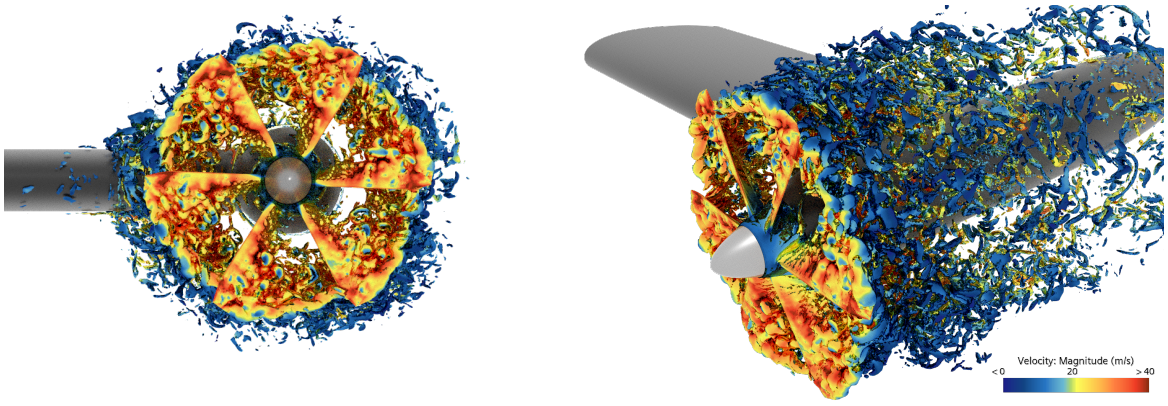

Figure 7: Instantaneous snapshots of vorticity isocontours colored by velocity magnitude, from LES simulation with a single propeller.

3.3.2. Propeller aerodynamic performance

Measured and numerically computed values of the time-averaged thrust and torque for the XPROP-S propeller are reported in Tab. 3. In the simulation, these values are obtained from time-averaged thrust and torque series over the last ten propeller rotations. The relative difference with respect to experimental results is of 5% for the thrust and 17% for the torque.

Table 3
Mean thrust and torque obtained experimentally and numerically for the single pylon-mounted XPROP-S propeller.

	Experiment [6]	Simulation (LES)
Mean thrust (N)	9.17	9.65
Mean torque (N.m)	0.288	0.338

3.4. Acoustic results

3.4.1. Tonal-Noise directivity

Acoustic directivity diagrams at the BPF and its first multiples are provided in Fig. 8 for the 90° antenna position of the experiment [5] (see antenna in Fig. 2(b)). As the sound emitted by the propeller includes both tonal and broadband components, the experimental Sound Pressure Levels (SPL), originally computed for a 1-Hz frequency resolution, have been calculated with the same frequency resolution as for the numerical spectra (58.3 Hz). This ensures a reliable comparison. Propeller noise is found to dominate over the noise emitted by the frame, which is expected as the propeller operates at zero-advance ratio, thus with a reduced impingement of the propeller slipstream on the pylon. Accounting for installation effects in the simulation overall leads to increased sound levels by 1 to 3 dB (especially at f = BPF), and to a better agreement with experimental data. More precisely, the FE-predicted noise levels are lower than the measurements by about 2-5 dB at f = BPF, whereas a good match with the experimental data is reported at f = 2BPF and f = 3BPF. The same conclusions are drawn farther away from the propeller plane, as shown by the results obtained for the antenna angle of 55°, reported in Fig. 9.

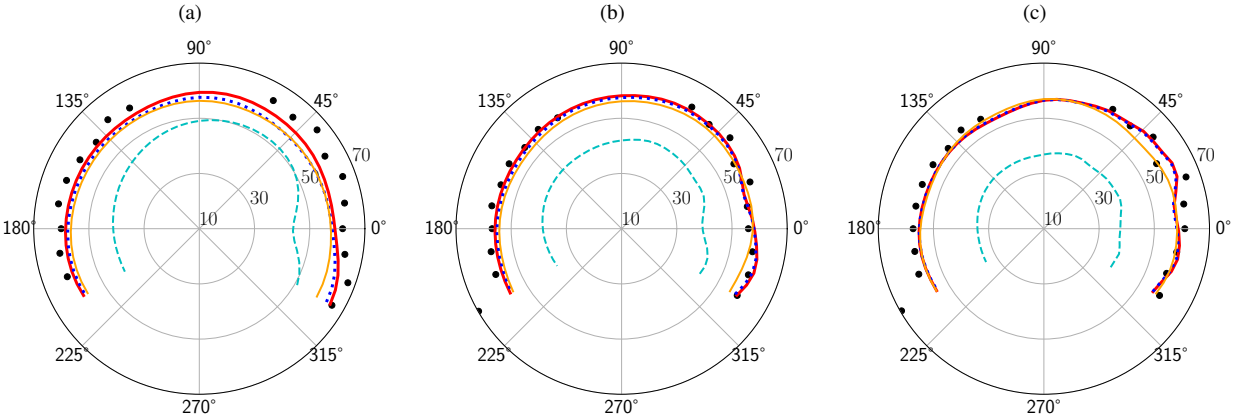

Figure 8: Directivities of the sound pressure levels for 90° antenna position in dB at (a) f = BPF, (b) f = 2BPF and (c) f = 3BPF: —— semi-analytical results for propeller in free field, FE results for ····· installed propeller, —— installed propeller+frame, – – – frame and • ECL experimental results [5].

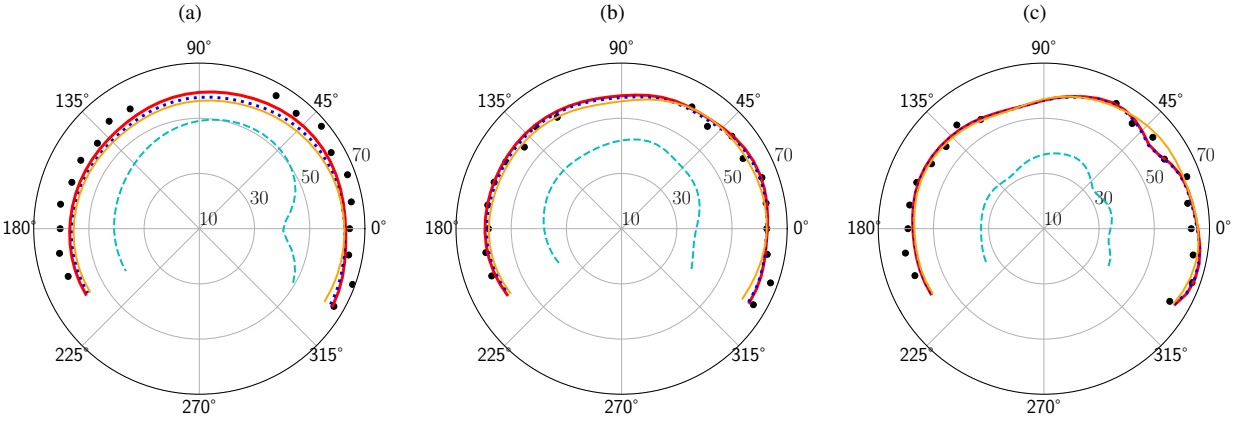

Figure 9: Directivities of the sound pressure levels for 55° antenna position in dB at (a) f = BPF, (b) f = 2BPF and (c) f = 3BPF: —— semi-analytical results for propeller in free field, FE results for ····· installed propeller, —— installed propeller+frame, – – – frame and • ECL experimental results [5].

In order to quantify the respective contribution of steady loading noise and unsteady loading noise, free-field and installed acoustic predictions have been computed by separating the steady and unsteady loading contributions in the definition of the rotating dipoles. The directivities of the sound pressure levels at the BPF for the 90° antenna position are presented in Fig. 10. Results are only shown at the BPF, as steady loading noise was found to be negligible at higher frequencies. Unsteady loading noise clearly dominates. In free field, directivities are relatively axisymmetric. Taking into account sound scattering by the frame, the axisymmetric directivity pattern is lost, steady loading noise is enhanced but does not significantly contribute to the total loading noise here. These results also suggest that scattering could make steady-loading noise dominant in other architectures or configurations.

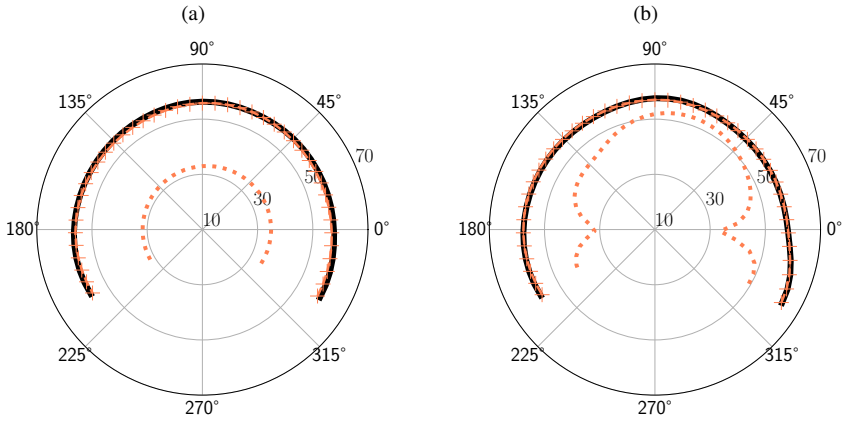

Figure 10: Directivities of the sound pressure levels in dB at f = BPF for the single propeller configuration for 90° antenna position at 0.1 m downstream of the rotor plane: (a) free-field propeller noise results and (b) propeller noise results including frame scattering. —— total loading noise, -+- unsteady loading noise and ····· steady loading noise.

3.4.2. Broadband acoustic spectra

The Power Spectral Densities (PSD) of the acoustic pressure obtained numerically at microphones 4, 10 and 17 of 90° antenna are presented as functions of frequency in Fig. 11 (see microphone numbering in Fig. 2(b)). Numerical results, provided in free-field and installed conditions, are compared to measurements [5]. The measured spectra are characterized by two main humps, neither centered on the BPF nor on its multiples, but at about 550 Hz and 1.1 kHz. These humps are attributed to the fact that the wakes/tip-vortices of the propeller blades are slowly convected downstream in the zero-advance ratio case, and thus have non-zero relative angular motion, up to the neighboring blades (see Fig. 7). The free-field numerical PSDs also feature the broad humps, but with a lower amplitude compared to the measurements. Including installation effects in the simulation leads to humps of amplitudes 2-3 dB higher, and thus a better agreement with the test results. At higher frequencies beyond 3 kHz, broadband noise, which is likely to be blade trailing-edge noise [5], dominates. It is rather well predicted by the free-field numerical approach up to 6 kHz, which is expected to be the mesh cut-off frequency of the CFD simulation. Finally, the low sound levels obtained for the frame-alone acoustic simulation confirm that frame self noise remains of secondary importance in this configuration.

4. Application to distributed XPROP-S propellers

Since the agreement between the test and simulation results is satisfactory for a single pylon-mounted propeller, the applicability of the present hybrid numerical approach to a two-propeller configuration representative of DEP architectures for aircraft is investigated in this section. This allows to focus on the contribution from propeller-propeller aerodynamic interaction, by comparing with what a simple superposition of individual propeller signatures would produce, only accounting for the aforementioned potential interactions with the frames.

4.1. Description of the two-propeller configuration

The DEP configuration reproduces the ECL experimental setup described in the references [5, 6] without the wing. The two propellers are synchronized with zero relative phase angle and mounted side-by-side on their frame,

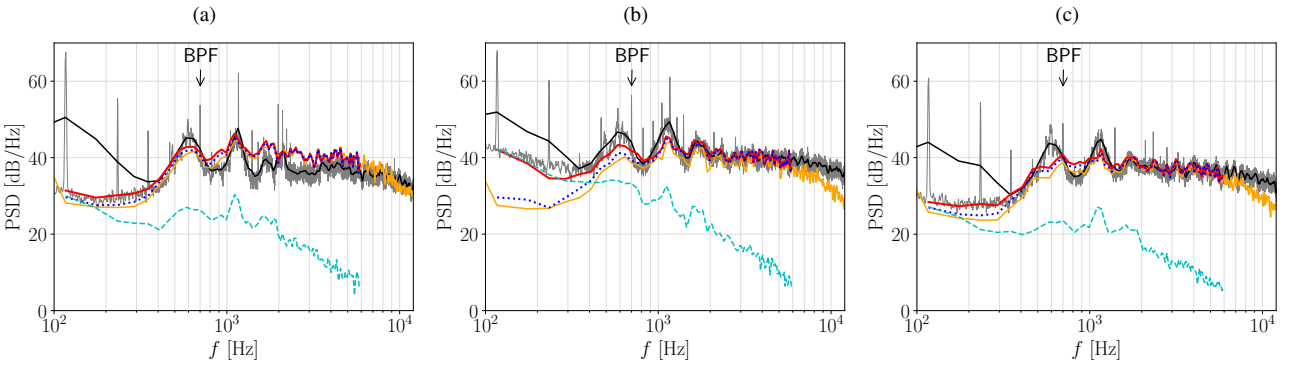

Figure 11: Power spectral densities of the acoustic pressure at (a) microphone 4, (b) microphone 10 and (c) microphone 17 for 90° antenna position: —— semi-analytical results for propeller in free-field, FE results for ····· installed propeller, —— installed propeller+frame, - - - frame, and ECL experimental results with —— resolution of 58 Hz and —— resolution of 1 Hz [5].

as illustrated in Fig. 1. The spanwise distance between the propeller axes is of $1.03D = 0.21$ m, corresponding to the shortest distance of 6 mm between blade tips. This is the most compact configuration studied in the experiment, for which maximum propeller-propeller interaction is expected. The configuration is studied at zero advance ratio for a rotational speed of 7000 rpm, as for the single-propeller case. This arrangement corresponds to the operating point 58 of the ECL experimental database published in Zenodo [6].

In the ECL investigation of the two-propeller configuration [5], the 90° microphone antenna position shown in Figs. 1, 2(b) and 2(c) lies 0.01 m downstream of the rotor plane, significantly closer to this plane compared to the single propeller configuration. Close to the rotor plane, it is well-known that the acoustic field can be very sensitive to small variations of the antenna position. Therefore, for the DEP configuration, acoustic results are systematically presented for the antenna positions at 55°, 90° and 135°, according to the schematic of Fig. 2(c).

4.2. Numerical setup

4.2.1. LES setup

The flow simulation is carried out following the same LES strategy as for the single-propeller case in Sec. 3. With two propellers, it leads to a polyhedral CFD mesh of 52 M cells. About five propeller revolutions are simulated to initialize the flow simulation. Aerodynamic data to be used as inputs in the acoustic simulations are then recorded for a period of twelve revolutions at a sampling frequency of 84 kHz. About 235 000 CPU hours have been used for this LES simulation, performed on AMD EPYC 7532 ROME CPU processors using 768 compute cores. As for the single-propeller case, it is important to note that the simulation setup has not been optimized to minimize the computational time.

4.2.2. Finite element simulation setup

For the acoustic predictions, three configurations are studied, as illustrated in Fig. 12: (a) two propellers radiating in free-field without scattering surface, (b) two propellers radiating in the presence of the frames, only considered as scattering surfaces, and (c) two propellers radiating in the presence of the frames and the wind tunnel nozzle as scattering surfaces. Note that frame self-noise is discarded here as its contribution has been shown negligible in Sec. 3.

The FE domains for the three configurations are presented in Fig. 13, together with three circles featuring the positions of the microphone antenna at 55°, 90° and 135°. Again, the propeller noise sources are computed adopting a blade segmentation based on 24 dipoles per blade to accurately model sound sources up to 12 kHz. The FEMAO simulations without nozzle are carried out up to 6 kHz. The simulation with nozzle, more memory demanding, is carried out up to 4.9 kHz. The sizes of the mesh elements are chosen small enough so that the polynomial orders do not exceed 10. The memory requirements for the two-propeller FEMAO simulations are provided for the highest frequency of interest in Tab. 4. The most computationally expensive simulation (with nozzle) requires 271 Gb to solve the FE problem at 4.9 kHz.

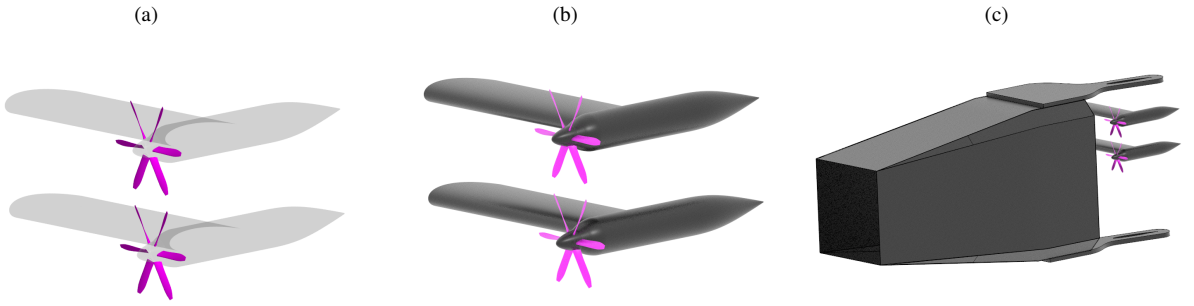

Figure 12: Views of three configurations selected for acoustic simulations of the two-propeller configuration, with aerodynamic sources indicated in purple: (a) propeller noise in free-field, (b) propeller noise and frames as scattering surfaces, (c) propeller noise and frames+wind tunnel nozzle as scattering surfaces.

Analytical free-field predictions performed from Eq. (4) up to 12 kHz where shown in an excellent agreement with the free-field FE results. The comparison is not shown here for the sake of brevity.

Table 4
Information about in-core solver memory requirements and maximum FEMAO order for acoustic simulations with the two propellers.

Configuration	Max frequency $f_{\max}$	Required memory (RAM) at $f_{\max}$	Max order p_{FEM}
2 propellers in free-field	5950	198 Gb	9
2 propellers with frames as a scattering surfaces	5950	214 Gb	10
2 propellers with frames+nozzle as scattering surfaces	4900	271 Gb	10

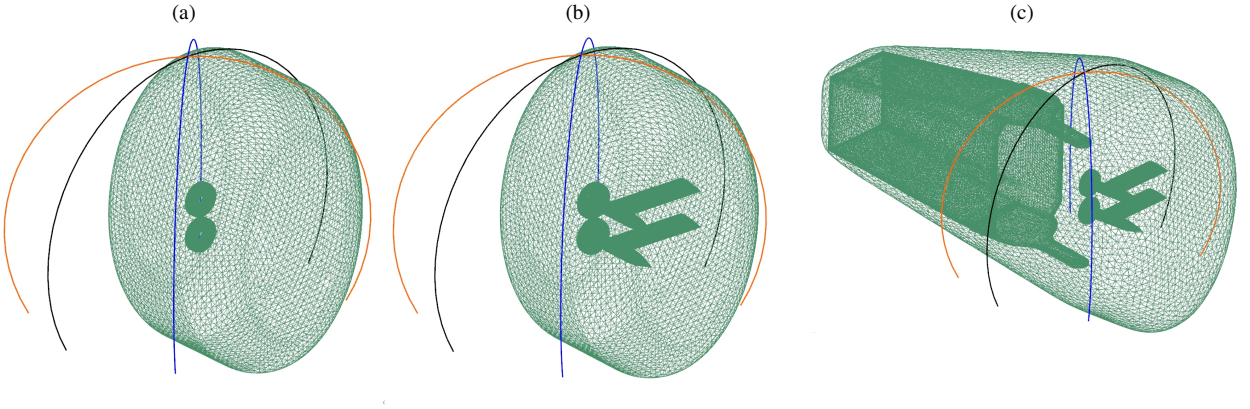

Figure 13: Views of three FE domains for the ECL DEP configuration: (a) two propellers in free field, (b) two pylon-mounted propellers and (c) two pylon-mounted propellers with nozzle. The microphone arcs at 55°, 90° and 135° are indicated in orange, black and blue, respectively.

4.3. Aerodynamic results

4.3.1. Flow instantaneous and time-averaged views

Instantaneous views of the vorticity iso-contours colored by the velocity magnitude are represented in Fig. 14. As for the single-propeller, tip vortices tend to stay in the vicinity of the propeller plane, instead of being strongly convected downstream of the propellers. The front view (Fig. 14(a)) exhibits a clear default of axisymmetry in the development

of the vortical patterns, which suggests mutual aerodynamic interaction, in addition to the deformation induced by the pylons. In the present co-rotating combination, opposite blade-tip motions in the area between the propeller discs generate increased shear, especially because of the 0°-phasing.

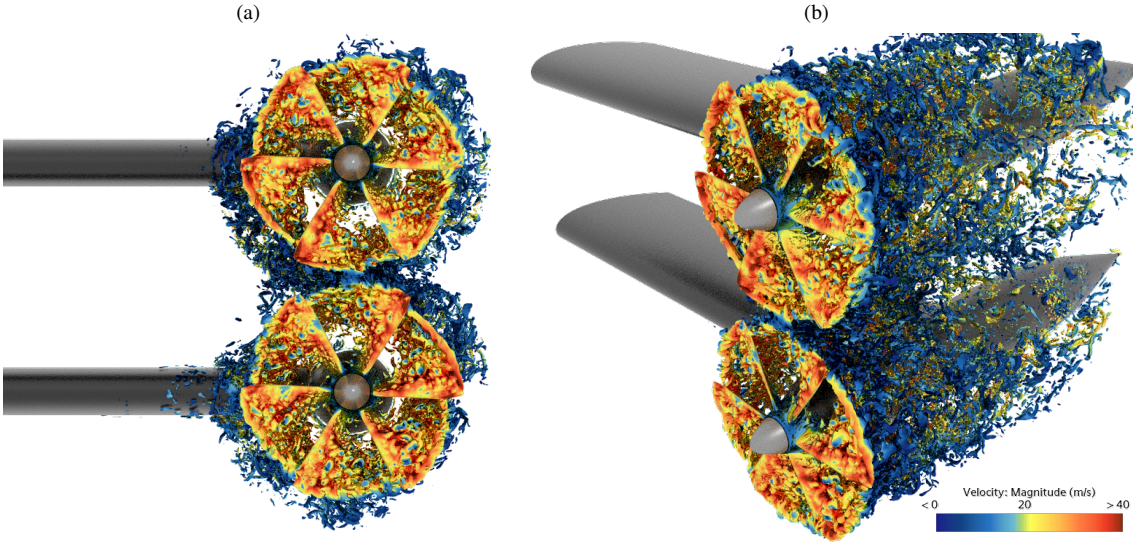

Figure 14: Instantaneous snapshots of vorticity iso-contours colored by velocity magnitude, from LES simulation with two propellers.

The mean-flow distortion resulting from the side-by-side operation of the pair of propellers is better highlighted when considering the time-averaged axial-velocity maps extracted upstream and downstream of the rotor plane, and shown in Fig. 15. The maps for the single propeller, also shown for comparison, are almost axisymmetric, suggesting that the potential interaction with the pylon is not a dramatic effect on the scale of the plots. In the upstream extraction plane of the DEP system, Fig. 15(b), a significant axial fluid motion is induced between the propellers, on the one hand, and large anti-symmetric orange patterns are seen, on the other hand. These features result from the opposite motions of blades of the two propellers as they approach to minimum distance from each other, and characterize the complex structure of the combined suction flows. It is remarkable that the distortion contaminates a large area of the propeller slipstreams. The distortion is also clearly visible in the downstream extraction plane, in the form of two protrusions, and of the similar anti-symmetric large areas with dark-red traces, as shown by Fig. 15(d).

4.3.2. Propeller aerodynamic performance

The measured and numerically predicted time-averaged thrust and torque for the two XPROP-S-propeller configuration are reported in Tab. 5. In the simulation, these results are obtained by averaging the thrust and torque values over the last ten propeller rotations. The simulation predicts a thrust of 9.73 N and a torque of 0.333 N.m for the two propellers. Experimentally, a similar thrust ($T = 9.71$ N) is obtained for the bottom propeller, while a much higher value is obtained for the top propeller. This high value is unexpected and could be attributed to a load cell calibration issue encountered during the test campaign. The measured torque values are about 30% higher than those of the simulations. This relatively large discrepancy remains unexplained.

Compared to the results reported for the isolated propeller configuration in Tab. 3, the thrust obtained from LES for the DEP configuration slightly increases by 0.8%. The torque is reduced by 1.5% in the DEP configuration. These results suggest that the mean thrust and torque are therefore not significantly affected by the short separation distance between the propellers. A similar observation was made by Zhou et al. [2] in their experimental study of small two-bladed twin rotors.

4.3.3. Blade-force signals

The time series of the axial, tangential and radial components of the propeller blade force are presented in Fig. 16, for the single-propeller and the DEP configuration, in order to highlight differences in the loading-noise source terms.

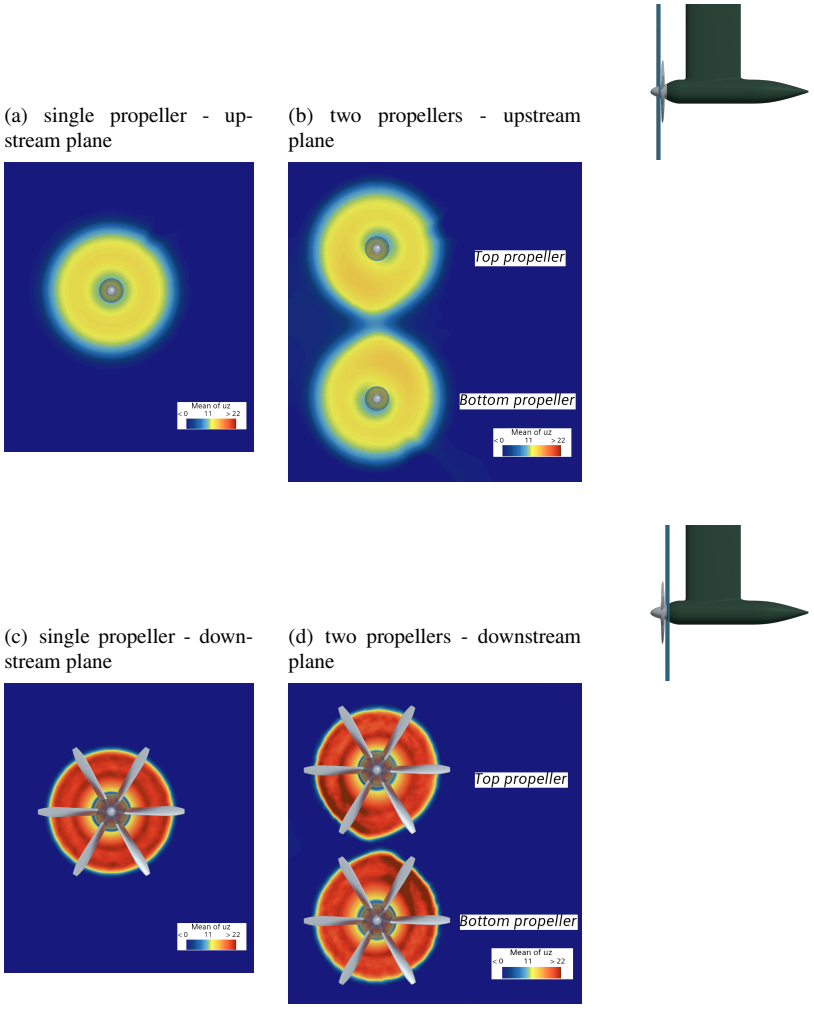

Figure 15: Time-averaged axial velocity maps in extraction planes located $0.073D$ upstream and downstream of the rotor plane and sketched on the right side. Color scales: 0-22 m/s.

Table 5
Mean thrust and torque obtained experimentally and numerically for the two pylon-mounted XPROP-S propellers.

	Experiment [6]	**Simulation (LES)**
Mean thrust - propeller bottom (N)	9.71	9.73
Mean torque - propeller bottom (N.m)	0.476	0.333
Mean thrust - propeller top (N)	13.86	9.73
Mean torque - propeller top (N.m)	0.466	0.333

These signals were computed by integrating the incompressible pressure data on the surface of a blade. Therefore, they must be understood as global information on sources, more condensed than the exact source terms per segment considered for acoustic predictions. For the sake of conciseness, signals are only shown for one blade; a similar behavior is observed for the other blades. In the DEP configuration, blade loading force components exhibit periodic, large-amplitude oscillations at the shaft frequency. Furthermore, for each force component, a delay of half a revolution is observed between the two propellers of the DEP arrangement. Such oscillations are not observed for the single-propeller configuration. They are attributed to propeller-propeller aerodynamic interactions. Similar oscillations are

reported in the literature for small propellers. In particular, blade force oscillations were observed by Zarri et al. [8] for three distributed XPROP-S propellers immersed in a 30 m/s flight stream and featuring a separation distance d (tip-to-tip distance) of $0.02D$, with D the propeller diameter. Lee [3] also obtained such oscillations for in-flight DJI 9443 2-blade propellers operating with a separation distance $d < 0.4D$. Zhou et al. [2] also observed these oscillations experimentally as the propeller separation distance decreases, typically for $d = 0.05D$ in their study. These blade force oscillations are expected to enhance unsteady loading noise and thus the total noise footprint.

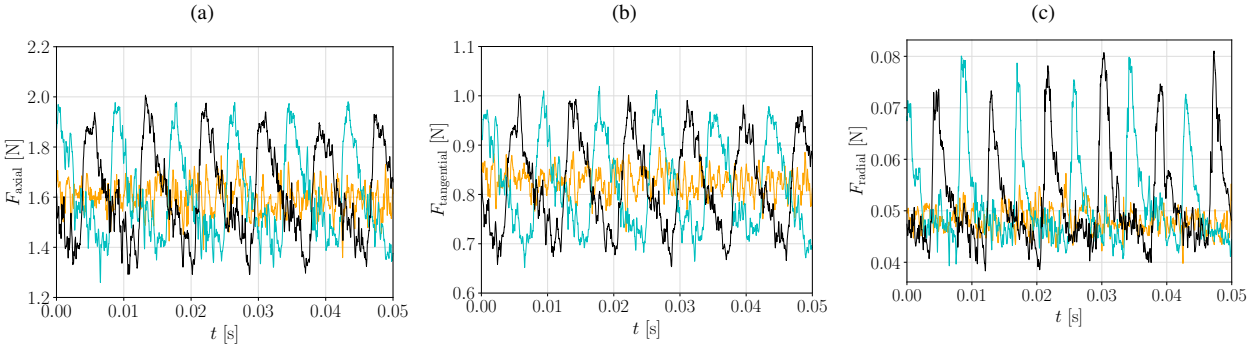

Figure 16: Time evolution of propeller blade forces in the (a) axial, (b) tangential and (c) radial directions for one single blade: —— isolated propeller, —— bottom propeller of DEP configuration and —— top propeller of DEP configuration.

For completeness, the force spectra averaged over the six blades are presented in Fig. 17, for the single propeller and the DEP configuration. The spectra computed per blade are also shown to highlight the blade-to-blade differences and provide an indication of the statistical convergence of the results. At low frequencies, the DEP exhibits significantly higher PSD values compared to the isolated propeller, with a maximum at the shaft frequency. These high PSD values are due to the propeller-propeller aerodynamic interactions. At mid and high frequencies ($f > 700$ Hz), similar spectra are obtained for the three components. This behavior is attributed to propeller self-noise sources, including propeller wake and blade-tip interactions.

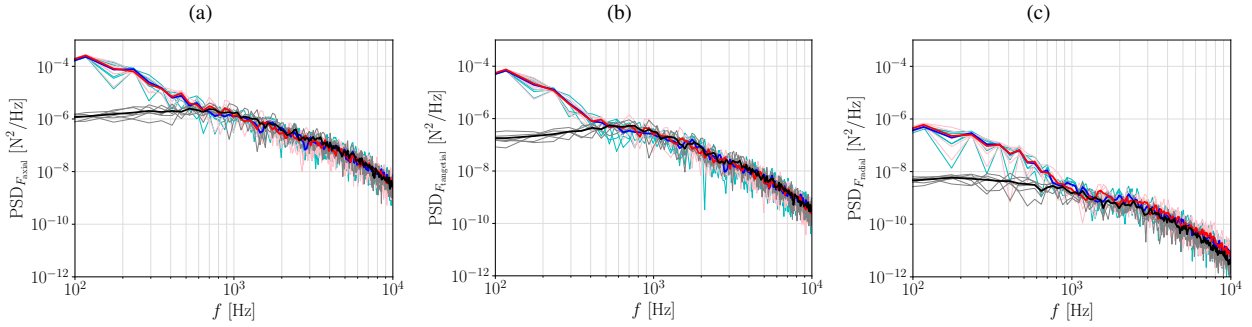

Figure 17: Spectra of the blade forces for —— the isolated propeller, —— the top propeller and the —— bottom propeller of the DEP configuration in the (a) axial, (b) tangential and (c) radial directions: (—— , —— , ——) results averaged over the six blades and (—— , —— , ——) results per blade.

4.4. Acoustic results

4.4.1. Installation effects in acoustic simulations

Sound directivity plots at the BPF and its first multiples are provided in Fig. 18 for the 90°, 55° and 135° antenna positions in the experiment [5]. Three computations are compared to the measurements, namely the free field of the propellers, the radiated field including scattering by the frames only, and the total field also considering scattering by the nozzle, as depicted in Fig. 12. The highest noise levels are obtained at the BPF. A good match between the

numerical and experimental directivities is observed, except at the BPF for the 90° antenna position where predicted sound levels are globally lower than the measurements. This can be explained by the fact that the 90° antenna in the DEP configuration is close to the rotor plane where the acoustic field can be sensitive to small variations of the antenna position. The numerical results reveal that acoustic installation effects do not significantly contribute to noise at the BPF and its first multiples, except for the 90-deg antenna at the BPF. In particular, including the nozzle as a scattering surface has almost no effect on the sound predictions, apart from the top part of the directivity diagrams. This result is of primary importance, because it also validates the experimental setup for the study of installation effects, for all measuring angles far enough from the antenna axis. Indeed, in the project, the setup was initially aimed at assessing the masking effect of a wing placed vertically; it would not be relevant, were the effect of the nozzle more significant.

The PSD of the acoustic pressure computed from the experimental and numerical signals are compared in Fig. 19. Results are shown at microphones 4, 10 and 17 for the 90°, 55° and 135° antenna. The results obtained from the simulations with installation effects are in fair agreement with the measurements. Over the frequency range 300 Hz-2 kHz, the benefits of accounting for the frame scattering to get improved predictions can be clearly seen compared to free-field conditions. This is particularly visible for the microphone 10 at the 90° arc position (Fig. 19(b)). It must be kept in mind that the equivalent sources of pylon scattering are dipoles normal to its surface. As such, they cannot radiate in the horizontal mid-plane of a pylon. This makes them poorly contributing *a priori* at microphone 4 and 17.

The fact that installation effects are more important at the BPF than at higher harmonics is explained by the modal structure of the tonal noise, on the one hand, and by the short distance between blade tips and the trailing edge, on the other hand. Tonal noise sources are expandable as a sum of equivalent source-modes, each of which is a circular distribution of plus and minus dipoles of zero instantaneous sum. The radiated sound is non-zero because of different distances from the constitutive elements of a mode to the observer. Yet in free field, some of these modes are efficient and some others only induce evanescent waves in the surrounding medium, as discussed by Roger & Kucukcoskun [29]. Furthermore, as a point dipole is approached at small distance of a scattering edge compared to the acoustic wavelength, its radiation is increasingly enhanced, which can be mathematically proven an asymptotic property of the Green's function tailored to the edge [30]. In the case of a source-mode, the closest constitutive elements to the edge have their contribution significantly more amplified, which induces an imbalance in the circular distribution of plus and minus. The net effect on an evanescent mode is to make it efficient, whereas the radiated power of an already efficient mode is nearly unchanged. Now, for the same source-to-edge distance, compactness is more pronounced at lower frequencies. This explains why the BPF is more affected than higher harmonics. More precisely, the wavelength at BPF is of 48 cm, which leads to a reduced wavenumber kr_0 of about 0.13 for a distance r_0 of 1 cm representative of blade tips, where k is the wavenumber. This is indeed in the range of reported amplification effect in the reference [30]. Larger values at higher harmonics are less subjected to the amplification. The presently observed installation effect exemplifies the compact regime of edge scattering.

4.4.2. Effect of propeller-propeller aerodynamic interactions on noise

The set of computed results is now exploited to get further insight into the influence of propeller-propeller aerodynamic interactions on the noise footprint, by either considering them in addition to the potential effect of the frames, or discarding them. For this, a complementary acoustic simulation is performed, following a simplified approach, applied by the authors in a recent study [24]. The simulation is achieved by using the propeller aerodynamic loads from the single-propeller CFD simulation and simply duplicating them to mimic the presence of a second propeller. The installed configuration of Fig. 12(b) is selected for the FE simulation, only featuring the two propeller frames as scattering surfaces.

This simplified numerical approach based on source duplication is actually tempting because it allows to save computational time. Indeed, only a single propeller needs to be included in the CFD simulation instead of two (and even more in the case of DEP systems made of multiple propulsive units). It is thus particularly desirable for optimization studies of the propeller-propeller separations/installations, where only a very limited number of configurations can be completely simulated due to the computational cost of the high-fidelity CFD flow simulations. In the present test, the validity of the simplified approach is assessed by comparing the sound predictions it provides with the ones obtained from the complete two-propeller CFD and associated acoustic simulation.

Sound directivities at the BPF and at 2BPF, as predicted with the exact computation and the duplication approach, are presented and compared to the measurements in Fig. 20 for the 90°, 55° and 135° antenna positions. For this DEP configuration with propellers in close proximity, ignoring propeller-propeller aerodynamic interactions leads to clearly underestimated sound levels, especially at the BPF. This is explained by the fact that the large periodic blade loads

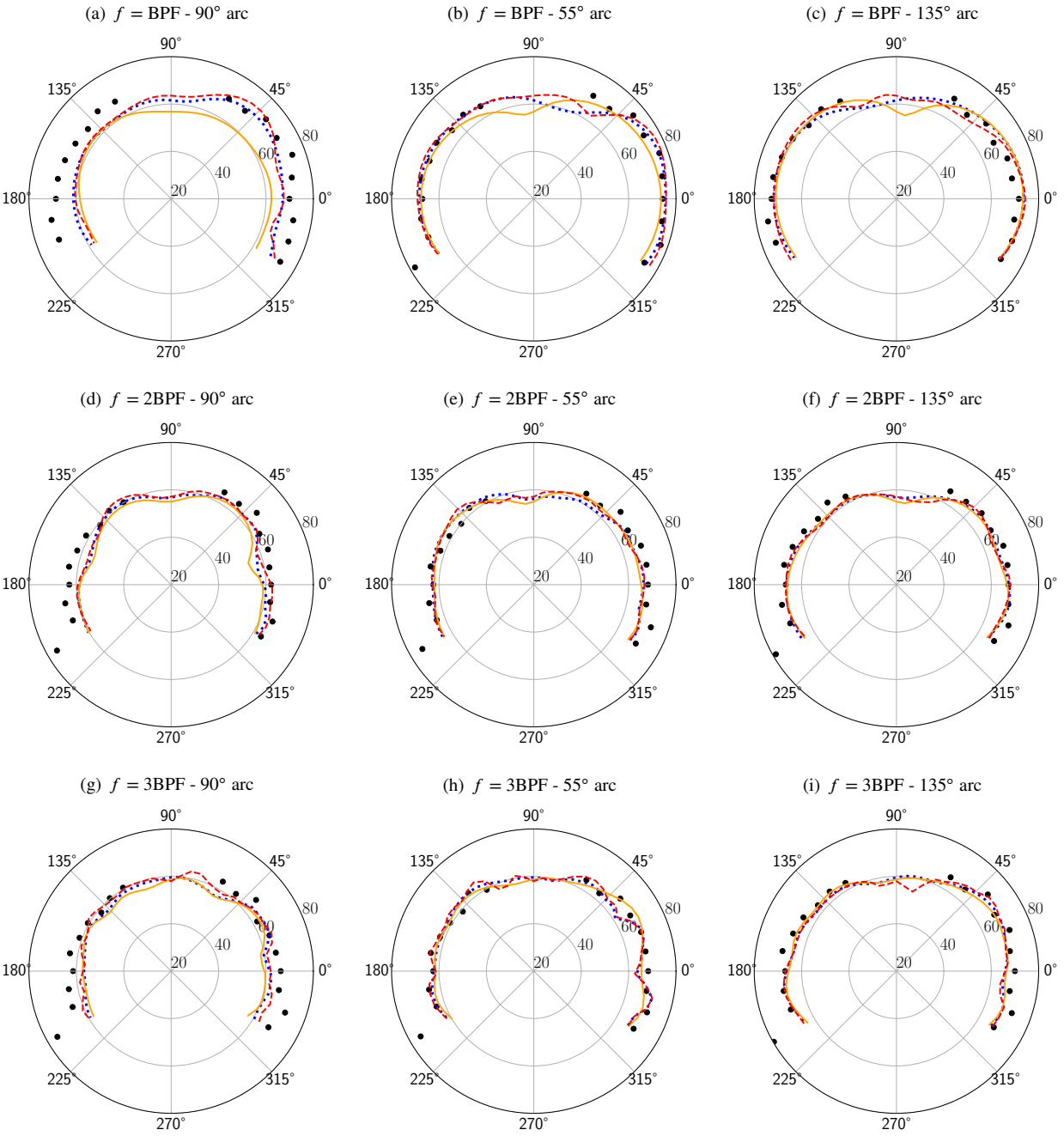

Figure 18: Directivities of the sound pressure levels for 90°, 55°, and 135° antenna positions in dB for the DEP configurations at (a)(b)(c) f = BPF, (d)(e)(f) f = 2BPF and (g)(h)(i) f = 3BPF: —— free-field semi-analytical results, ····· frame-scattering FE results, – – – frame-nozzle scattering FE results and • ECL experimental results [5].

evidenced in Fig. 16 cannot be reproduced in the single-propeller CFD simulation. The comparison highlights the need of explicitly accounting for the two propellers in the flow simulation to accurately capture the noise sources.

To give further insight into the noise generation mechanisms, the respective contributions of steady loading noise and unsteady loading noise are computed separately. The FE propeller noise directivities including frame scattering at the BPF are presented in Fig. 21 for the 90° antenna position. Unsteady loading noise clearly dominates over steady

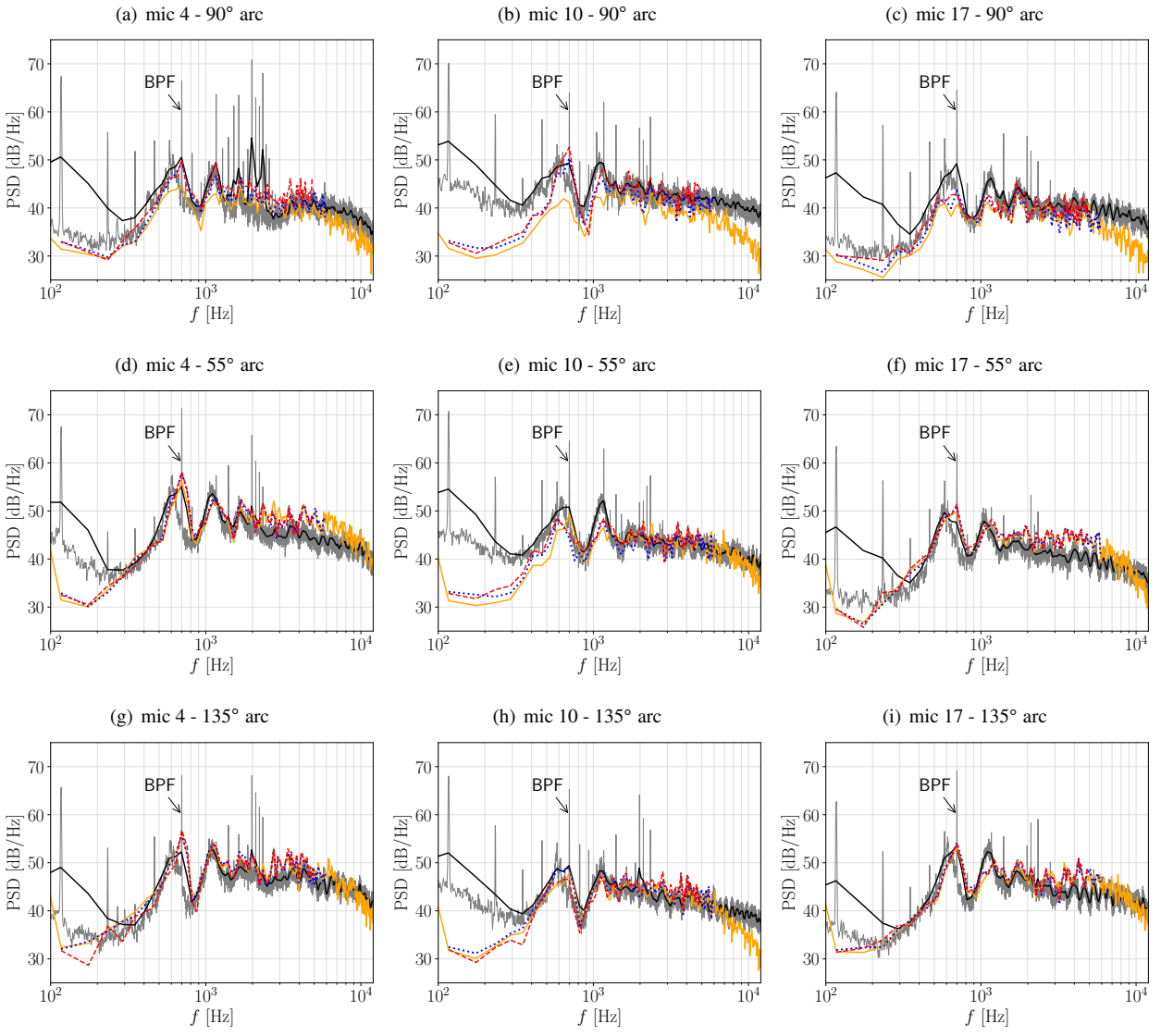

Figure 19: Power spectral density of the acoustic pressure at (a)(d)(g) microphone 4, (b)(e)(h) microphone 10 and (c)(f)(i) microphone 17 for 90°, 55° and 135° antenna positions of the DEP configuration: —— semi-analytical results for propeller in free-field, ····· frame-scattering configuration, – – – frame-nozzle scattering configuration, and ECL experimental results with —— resolution of 58 Hz and —— resolution of 1 Hz [5].

loading noise. Discarding propeller-propeller aerodynamic interactions only affects the unsteady loading noise. The same trends have been observed at other positions of the microphone antenna (results not shown here for the sake of conciseness).

Finally, directivities at 1 m from the propellers are extracted from the finite-element simulations in two additional planes: the vertical plane corresponding to the meridian plane containing the axis of the propellers, parallel to the stream direction and the horizontal plane located at the middle between propeller axes, as illustrated in Fig. 22(a). Such results are not accessible in the experiment but provide useful information about the positions where interaction and installation effects are predominant. Total loading noise results with frame acoustic scattering are presented in Figs. 22(b) and 22(c) from both the exact computation and the duplication approach. Results obtained from free-field acoustic propagation are also included. Propeller-propeller aerodynamic interactions lead to a significant increase in the sound levels. The acoustic installation effect only plays a role near the rotor plane.

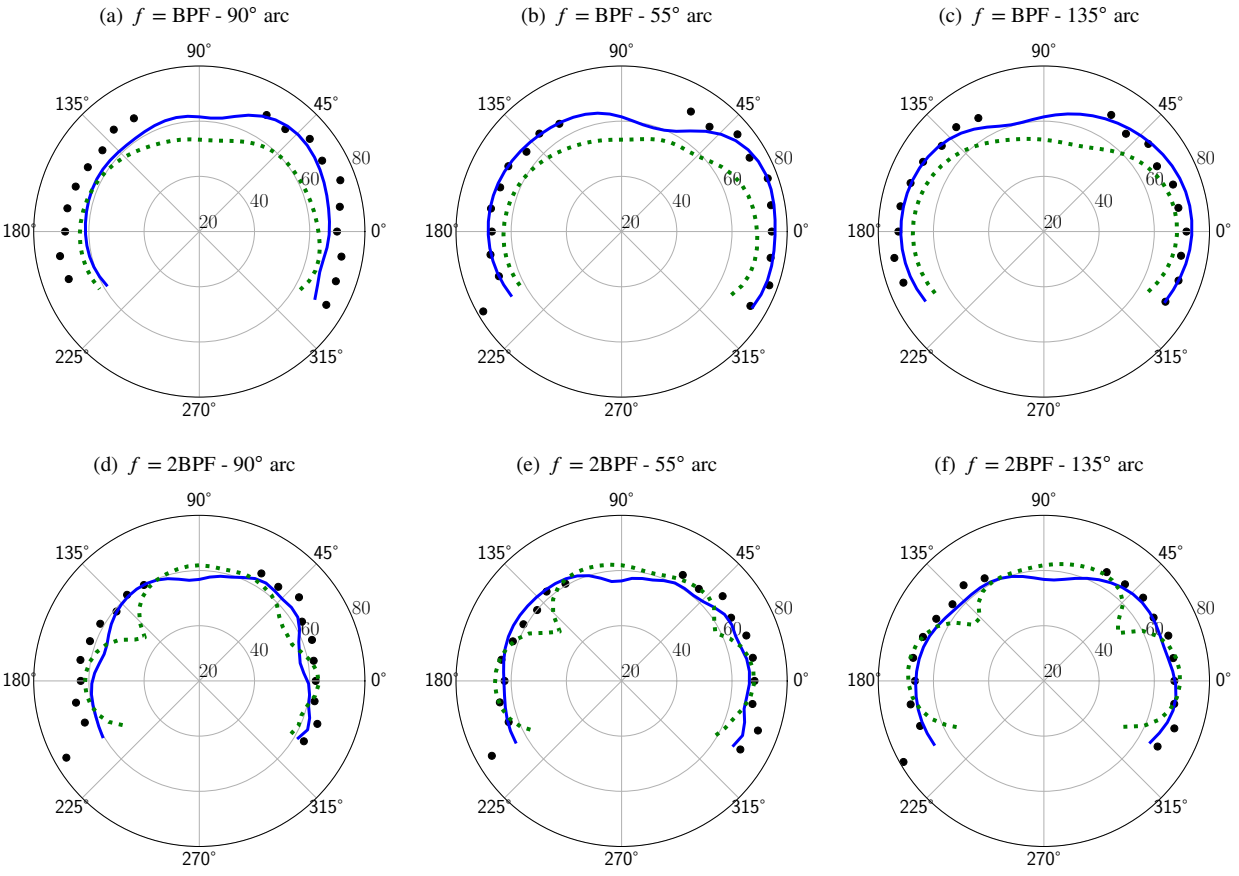

Figure 20: Directivities of the sound pressure levels for 90°, 55°, and 135° antenna positions in dB for the DEP configurations at (a)(b)(c) f = BPF and (d)(e)(f) f = 2BPF: FE propeller noise results including frame scattering —— from two-propeller flow simulation, ····· from single-propeller flow simulation + propeller sound source duplication, and • ECL experimental results [5].

5. Conclusions

This study demonstrates the capability of an aeroacoustic hybrid numerical approach, based on incompressible large-eddy simulation and acoustic high-order finite-element simulations, to predict the tonal and broadband noise radiated by a low-Reynolds number two-propeller configuration at zero advance ratio previously studied experimentally at École Centrale de Lyon.

The performance of the numerical approach is first verified by simulating a single pylon-mounted XPROP-S propeller, also characterized experimentally. The numerical results show a good agreement with the experimental data. In particular, the sound levels at the blade passing frequency and its first multiples are fairly well predicted. The main characteristics of the broadband noise spectra, including the broads humps of the propeller noise in the range 3-5 kHz, are also captured in the simulations.

In a second part of this study, the simulation strategy is applied to the ECL distributed electric propulsion configuration made of two co-rotating XPROP-S propellers synchronized and mounted side-by-side on their frames. The high-fidelity flow simulation is carried out including the two propellers to account for propeller-propeller aerodynamic interactions. Again, numerical results show a fair agreement with experimental data. Propeller-propeller aerodynamic interactions are found to significantly contribute to the noise footprint. This is attributed to the unsteady loading noise associated with periodic propeller loads, not observed for the single-propeller case. Additionally, accounting for installation effects in the acoustic simulations is found to improve the noise prediction over the frequency range 300 Hz-2 kHz.

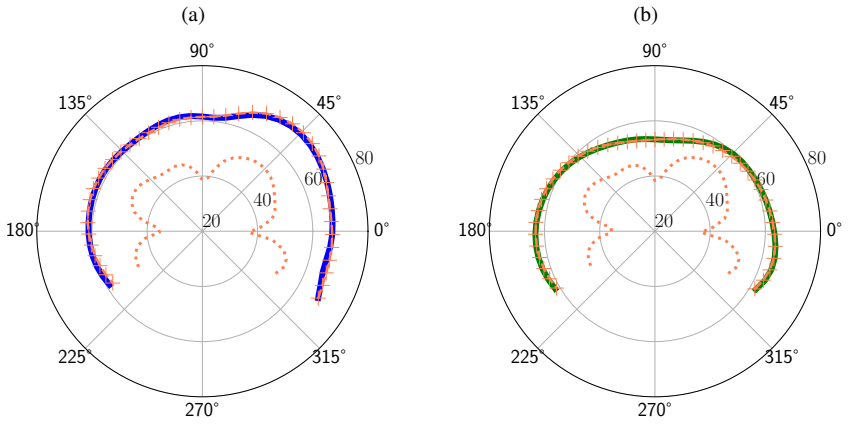

Figure 21: Directivities of the sound pressure levels in dB at f = BPF for 90° antenna position at 0.01 m downstream of the rotor plane for the DEP configuration: FE propeller noise results including frame scattering (a) from two-propeller flow simulation, and (b) from single-propeller flow simulation + propeller sound source duplication: —— total loading noise, -+- unsteady loading noise and ····· steady loading noise.

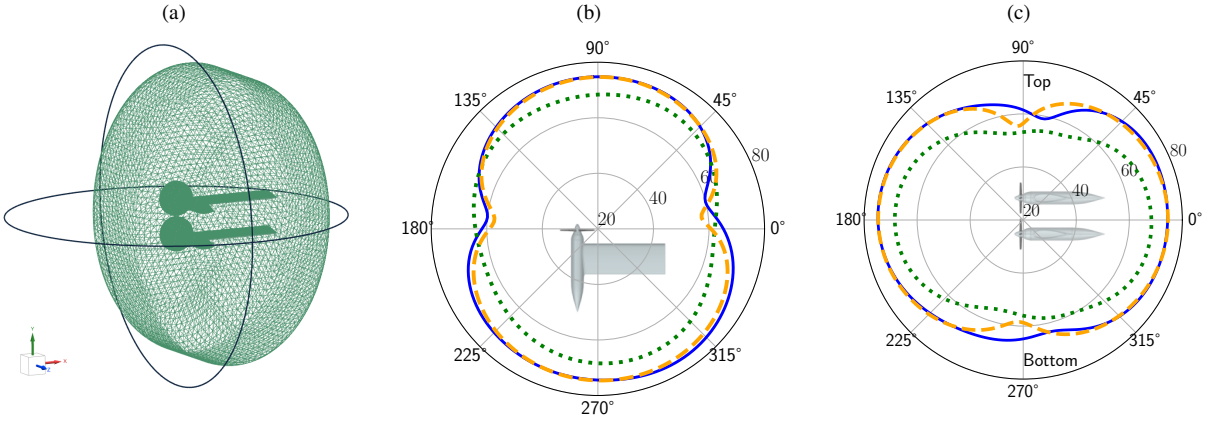

Figure 22: (a) View of the horizontal and vertical circles where directivities are computed and directivity of the sound pressure levels at f = BPF for (b) horizontal circle and (c) vertical circle: FE propeller noise results – – – from two-propeller flow simulation with free-field acoustic propagation, —— from two-propeller flow simulation with frame acoustic scattering, ····· from single-propeller flow simulation and sound source duplication.

In order to further highlight the relative contribution of propeller-propeller aerodynamic interactions on noise, sound predictions have been computed with a simplified numerical approach discarding the interactions. This approach is based on a single-propeller flow simulation and a sound source duplication to account for the presence of the second propeller. With this simplified approach, a strong under-prediction of the noise levels compared to the measurements is reported. The results confirm that the simplification, particularly attractive for the assessment of various DEP arrangements at low CFD computational cost within the scope of an optimization procedure, is abusive when the propellers are in too close vicinity to each other. Yet it could be retained for DEP systems, in which a larger propeller-propeller distance would prevent the presently observed strong aerodynamic interactions.

Acknowledgments

The authors gratefully acknowledge the European Commission for its support through the ENODISE project (Enabling optimized disruptive airframe-propulsion integration concepts, Horizon 2020 research and innovation

programme under grant agreement No 860103). The authors are also grateful to the Technische Universiteit Delft (TU Delft) for sharing the geometry of the XPROP-S propeller.

Appendices

A. CFD grid sensitivity study

The influence of the mesh resolution has been evaluated for the single-propeller configuration by performing three LES simulations using three meshes, referred to as coarse, medium and fine grids. They contain 14M, 28M and 36M cells, respectively.

The propeller performances predicted from the three LES are reported in Tab. 6. Using coarse grid, the relative difference with respect to experimental results is of 8 % for the thrust and 13 % for the torque. With the two finer meshes, thrust predictions get closer to the measurements, with relative differences of 5 % and 6 % for the medium and fine grids, respectively. For the torque, relative difference with the measurements of 17 % and 16 % are obtained for the medium and fine grids, respectively.

Table 6
Mean thrust and torque values obtained experimentally and numerically for the isolated pylon-mounted XPROP-S propeller.

	Experiment [6]	**LES coarse grid**	**LES medium grid**	**LES fine grid**
Mesh (total cells)	-	14M	28M	36M
Mesh (cells in rotating zone)	-	9M	11M	19M
Mean thrust (N)	9.17	9.94	9.65	9.71
Mean torque (N.m)	0.288	0.325	0.338	0.333

In order to obtain sound predictions, propeller sound sources have been computed from the CFD aerodynamic pressure data recorded over 10, 16 and 7 propeller revolutions respectively.

Acoustic results obtained using the three CFD meshes are compared at microphone 4 for the 90-deg and 55-deg antenna positions in Fig. 23. The spectra have been computed for a frequency resolution of 58.3 Hz. The LES with coarse and fine grids simulate shorter physical times compared to the LES with medium grid, leading to less statistically converged spectra in Fig. 23. The spectra obtained with medium and fine grids have similar shapes for $f \leq 7$ kHz. At higher frequencies, sound levels computed from the fine grid are higher than those found for the medium grid. Using coarse grid, much lower sound levels are obtained.

Based on the fact that similar aerodynamic and acoustic results are obtained from medium and fine grids, the medium grid has been selected for the aeroacoustic simulations presented in this study.

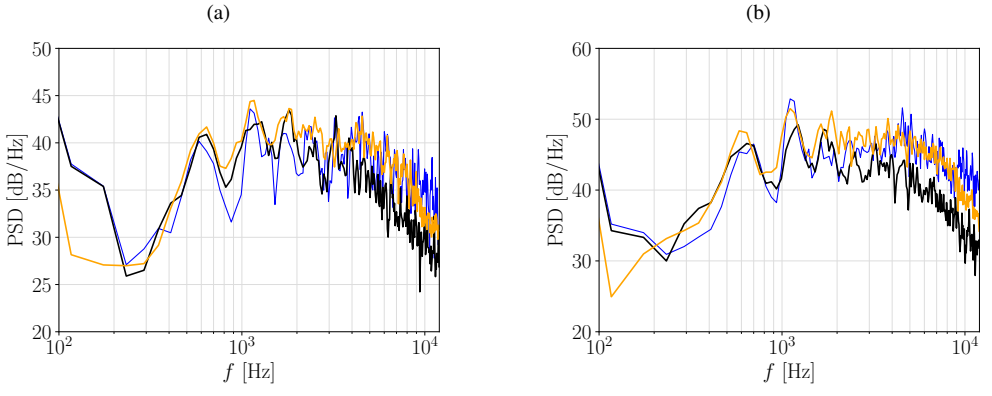

Figure 23: Power spectral density of the acoustic pressure at microphone 4 (a) for 90° antenna position and (b) for 55° antenna position: free-field analytical results obtained with —— coarse grid, —— medium grid and —— fine grid.

B. Comparisons of FE and analytical results

In order to verify the performance of the FE approach, numerical and analytical acoustic results in free field are compared at microphone 4 for the 90° antenna position in Fig. 24. The agreement between the FE results and the analytical solution is excellent.

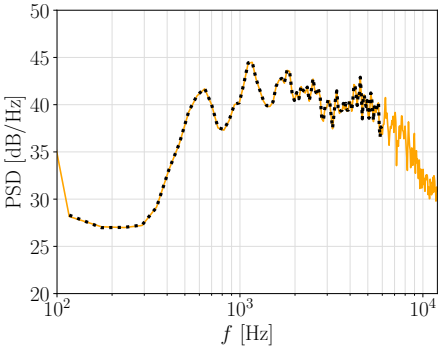

Figure 24: Power spectral density of the acoustic pressure at microphone 4 for 90° antenna position: —— analytical results for propeller in free-field and ····· FE results for propeller in free-field.

References

[1] P. F. Pelz, P. Leise, M. Meck, Sustainable aircraft design—a review on optimization methods for electric propulsion with derived optimal number of propulsors, Progress in Aerospace Sciences 123 (2021) 100714. https://doi.org/10.1016/j.paerosci.2021.100714.

[2] W. Zhou, Z. Ning, H. Li, H. Hu, An experimental investigation on rotor-to-rotor interactions of small uav propellers, in: 35th AIAA Applied Aerodynamics Conference, AIAA Paper 2017-3744, 2017. https://doi.org/10.2514/6.2017-3744.

[3] H. Lee, D.-J. Lee, Rotor interactional effects on aerodynamic and noise characteristics of a small multirotor unmanned aerial vehicle, Physics of Fluids 32 (4). https://doi.org/10.1063/5.0003992.

[4] R. de Vries, N. van Arnhem, T. Sinnige, R. Vos, L. L. M. Veldhuis, Aerodynamic interaction between propellers of a distributed-propulsion system in forward flight, Aerospace Science and Technology 118 (2021) 107009. https://doi.org/10.1016/j.ast.2021.107009.

[5] D. Acevedo-Giraldo, M. Roger, M. C. Jacob, Experimental study of the aerodynamic noise of a pair of pusher-propellers installed over a wing, in: AIAA Aviation 2023 Forum, AIAA Paper 2023-3359, 2023. https://doi.org/10.2514/6.2023-3359.

[6] D. Acevedo-Giraldo, M. Roger, M. C. Jacob, H2020 ENODISE: Experimental dataset configuration b2 ecl, https://zenodo.org/record/7925336 (2023).

[7] ENODISE Project (enabling optimized disruptive airframe-propulsion integration concepts), https://www.vki.ac.be/index.php/about-enodise, grant agreement number 860103 (2020-2024).

[8] A. Zarri, A. Koutsoukos, F. Avallone, F. de Prenter, D. Ragni, D. Casalino, Aerodynamic and acoustic interaction effects of adjacent propellers in forward flight, in: AIAA Aviation 2023 Forum, AIAA Paper 2023-4489, 2023. https://doi.org/10.2514/6.2023-4489.

[9] Z. Yang, M. Meinke, W. Schroeder, Numerical analysis of propeller-airfoil interaction in a distributed propulsion system using a hybrid les and fw-h approach, in: 30th AIAA/CEAS Aeroacoustics Conference, AIAA-Paper 2024-3211, 2024. https://doi.org/10.2514/6.2024-3211.

[10] J. E. Barker, A. Zarri, J. Christophe, C. F. Schram, Numerical investigation of tonal noise emissions from propeller-wing aerodynamic and acoustic interactions, in: AIAA AVIATION 2023 Forum, AIAA Paper 2023-4056, 2023. https://doi.org/10.2514/6.2023-4056.

[11] M. Terracol, E. Manoha, C. Herrero, E. Labourasse, S. Redonnet, P. Sagaut, Hybrid methods for airframe noise numerical prediction, Theoretical and Computational Fluid Dynamics 19 (2005) 197–227. https://doi.org/10.1007/s00162-005-0165-5.

[12] P. Martínez-Lera, C. Schram, H. Bériot, R. Hallez, An approach to aerodynamic sound prediction based on incompressible-flow pressure, Journal of Sound and Vibration 333 (1) (2014) 132–143. https://doi.org/10.1016/j.jsv.2013.08.033.

[13] G. Romani, E. Grande, F. Avallone, D. Ragni, D. Casalino, Performance and noise prediction of low-reynolds number propellers using the lattice-boltzmann method, Aerospace Science and Technology 125 (2022) 107086. https://doi.org/10.1016/j.ast.2021.107086.

[14] X. Li, H. Wu, Y. Li, P. Zhou, S. Zhong, X. Zhang, Z. Ma, Experimental study of the effect of boundary-layer transition on rotor aeroacoustics, AIAA Journal (2024) 1–8https://doi.org/10.2514/1.J063785.

[15] Siemens Digital Industries Software, Simcenter STAR-CCM+ (version 18.06.007-R8) (2023).

[16] A. Kierkegaard, A. West, S. Caro, Hvac noise simulations using direct and hybrid methods, in: 22nd AIAA/CEAS Aeroacoustics Conference, AIAA Paper 2016-2855, 2016. https://doi.org/10.2514/6.2016-2855.

[17] L. Erbig, S. Lardeau, Hybrid aeroacoustic simulation of eaa's axial fan benchmark, in: DAGA 2022 Stuttgart, Germany, 2022, pp. 360–363.

[18] A. Schell, V. Cotoni, Flow induced interior noise prediction of a passenger car, SAE International Journal of Passenger Cars - Mechanical Systems 9 (3) (2016) 1053–1062. https://doi.org/10.4271/2016-01-1809.

[19] L. Erbig, S. Landi, J. Cuenca, C. Colangeli, R. Hallez, O. Minck, M. P. J. Sanders, Rod-airfoil wind tunnel testing, a classic revisited: Validation of aeroacoustics numerical modelling in the near and far field, in: 30th AIAA/CEAS Aeroacoustics Conference, AIAA Paper 2024-3310, 2024. https://doi.org/10.2514/6.2024-3289.

[20] H. Bériot, A. Prinn, G. Gabard, Efficient implementation of high-order finite elements for Helmholtz problems, International Journal for Numerical Methods in Engineering 106 (3) (2016) 213–240. https://doi.org/10.1002/nme.5172.

[21] Siemens Digital Industries Software, Simcenter Nastran Acoustics User's Guide (version 2312) (2023).

[22] F. Nicoud, F. Ducros, Subgrid-scale stress modelling based on the square of the velocity gradient tensor, Flow, turbulence and Combustion 62 (3) (1999) 183–200. https://doi.org/10.1023/A:1009995426001.

[23] K. Kucukcoskun, A. Kierkegaard, Accuracy and advantages of hybrid solutions compared to direct noise calculations for low-speed fan noise, in: FAN2022 Conference, Universitäts-und Landesbibliothek Darmstadt, 2022. https://doi.org/10.26083/tuprints-00021708.

[24] S. Le Bras, K. Kucukcoskun, D. Acevedo-Giraldo, M. Roger, Aeroacoustic simulations of a pylon-mounted propeller configuration at low Reynolds number, in: 30th AIAA/CEAS Aeroacoustics Conference, AIAA Paper 2024-3101, 2024. https://doi.org/10.2514/6.2024-3101.

[25] J. E. Ffowcs Williams, D. L. Hawkings, Sound generation by turbulence and surfaces in arbitrary motion, Philosophical Transactions of the Royal Society of London. Series A, Mathematical and Physical Sciences 264 (1151) (1969) 321–342. https://doi.org/10.1098/rsta.1969.0031.

[26] M. Roger, Near-field fan noise modeling and installation effects due to scattering surfaces, in: Proceedings Fan Noise 2007 conference, 2007.

[27] H. Reichardt, Vollständige darstellung der turbulenten geschwindigkeitsverteilung in glatten leitungen, ZAMM-Journal of Applied Mathematics and Mechanics/Zeitschrift für Angewandte Mathematik und Mechanik 31 (7) (1951) 208–219. https://doi.org/10.1002/zamm.19510310704.

[28] H. Bériot, A. Modave, An automatic perfectly matched layer for acoustic finite element simulations in convex domains of general shape, International Journal for Numerical Methods in Engineering 122 (5) (2021) 1239–1261. https://doi.org/10.1002/nme.6560.

[29] M. Roger, K. Kucukcoskun, Near-and-far field modeling of advanced tail-rotor noise using source-mode expansions, J. Sound & Vib. 453 (2019) 328–354. https://doi.org/10.1016/j.jsv.2019.02.007.

[30] M. Roger, S. Moreau, K. Kucukcoskun, On sound scattering by rigid edges and wedges in a flow, with application to high-lift device aeroacoustics, J. Sound & Vib. 362 (2016) 252–275. https://doi.org/10.1016/j.jsv.2015.10.004.

CRediT authorship contribution statement

S. Le Bras: Conceptualization, Methodology, Software, Validation, Writing - Original draft preparation. **K. Kucukcoskun:** Methodology, Software, Writing. **D. Acevedo-Giraldo:** Conceptualization, Investigation, Methodology, Writing. **M. Roger:** Conceptualization, Methodology, Writing - Original draft preparation.

Declaration of competing interest

The authors declare that they have no known competing financial interests or personal relationships that could have appeared to influence the work reported in this paper.